Full-torus impurity transport simulation for optimizing plasma discharge operation using a multi-species impurity powder dropper in the large helical device

journal or publication title	Contributions to Plasma Physics
volume	60
number	5-6
year	2019-12-12
URL	http://hdl.handle.net/10655/00012668

doi: 10.1002/ctpp.201900101

Full-torus Simulation of Tungsten Erosion by Intrinsic Carbon Ions in the Large Helical Device Peripheral Plasma Using the ERO2.0 code

M. Shoji[1*], **G. Kawamura**[1,2], **J. Romazanov**[3], **A. Kirschner**[3], **S. Masuzaki**[1,2], **and S. Brezinsek**[3]

[1] National Institute for Fusion Science, National Institutes of Natural Sciences, Oroshi-cho, Toki, Gifu 509-5292 Japan

[2] Graduate University for Advanced Studies (SOKENDAI), Oroshi-cho, Toki, Gifu 509-5292 Japan

[3] Forschungszentrum Jülich GmbH, Institut für Energie- und Klimaforschung- Plasmaphysik, Jülich 52425 Germany

The closed helical divertor in one helical section in the Large Helical Device (LHD) has been recently replaced to a tungsten divertor configuration from the conventional carbon divertor one. The exfoliation and erosion of tungsten layers coated on the divertor plates were found in the closed helical divertor region. The reason for the tungsten erosion can be ascribe to the physical sputtering of tungsten by intrinsic carbon ions in the LHD peripheral plasma which are produced by the physical and chemical sputtering on the carbon divertor plates

installed in the other helical sections. For finding an effective measure for suppressing the tungsten erosion, the three-dimensional Monte-Carlo impurity transport and plasma-surface interaction code ERO2.0 was applied to the full-torus simulation of the erosion on the divertor plates in LHD. The simulation has successfully provided an effective measure for suppressing the tungsten erosion by replacing carbon divertor plates to tungsten ones in two critical divertor areas.

KEYWORDS tungsten, erosion, carbon, ERO2.0, EMC3-EIRENE, LHD

1 INTRODUCTION

Tungsten is regarded as the most promising candidate for divertor components in future nuclear fusion reactors because of its high threshold energy of sputtering and the low tritium inventory, etc [1, 2]. In the Large Helical Device (LHD) [3], upgrade to the tungsten divertor configuration from the conventional carbon divertor one has now progressed step by step for investigating the feasibility of the tungsten divertor plates in helical plasma confinement systems. One out of ten helical sections has been replaced to the tungsten divertor configuration since

the experimental campaign in FY2019. Tungsten coated divertor plates were installed in the closed helical divertor (CHD) region [4, 5] in one helical section (9-I) in the inboard side of the torus, which showed no serious degradation of the performance of plasma discharges, and the successful reduction of mixed-material deposition layers and dust formation in the divertor region [6]. However, after the experimental campaign, the exfoliation and erosion of tungsten coated layers on the divertor plates in the CHD region were found by an analysis using a glow discharge optical emission spectroscopy (GD-OES) [7]. It is believed that the tungsten erosion can be ascribed to the physical sputtering due to the intrinsic carbon ions in the LHD peripheral plasma. The carbon ions are produced by the physical and chemical sputtering on the conventional carbon divertor plates, which are installed in the other nine helical sections, due to background hydrogen and deuterium plasmas. The tungsten erosion is a critical issue for upgrading the divertor configuration from the conventional carbon divertor one. For finding an effective measure to suppress the tungsten erosion, the three-dimensional Monte-Carlo impurity transport and plasma-surface interaction code ERO2.0 [8] was applied using a full-torus model including the divertor components in the CHD region with the tungsten divertor plates installed in the one of ten helical sections.

In the next section, this paper describes the geometrical setup for the ERO2.0 simulation in the full-torus model. In section 3, for identifying the position of carbon sources causing the tungsten erosion, the simulations of the toroidal and poloidal distribution of the erosion on the carbon divertor plates are presented under the conditions

---

∗ Corresponding author. E-mail: shohji.mamoru@nifs.ac.jp, Phone: +81 572 58 2151, Fax: +81 572 58 2618

where the carbon source locally exists at one of six representative divertor positions in a full carbon divertor case. In section 4, the ERO2.0 simulation of the tungsten erosion profile on the tungsten divertor plates in the CHD region is shown, and the total tungsten erosion rates with and without effective measures for reducing the tungsten erosion are also presented. As a result, the simulation demonstrates effective measures for supressing the tungsten erosion in the closed helical divertor. Section 5 summarizes this paper.

2 FULL-TORUS SIMULATION OF THE EROSION PROFILE ON DIVERTOR PLATES USING ERO2.0

A three-dimensional full-tours model of LHD for the simulation is illustrated in Figure 1, which includes the vacuum vessel, the closed helical divertor with the tungsten divertor plates installed in the one helical section in the inboard side (9-I), and the conventional carbon divertor plates in the other divertor regions. These components consist of aggregates of small triangle surfaces which size is less than a few centimetres. The toroidal and poloidal distribution of carbon and tungsten erosion on the divertor plates in the full-torus model is calculated using the

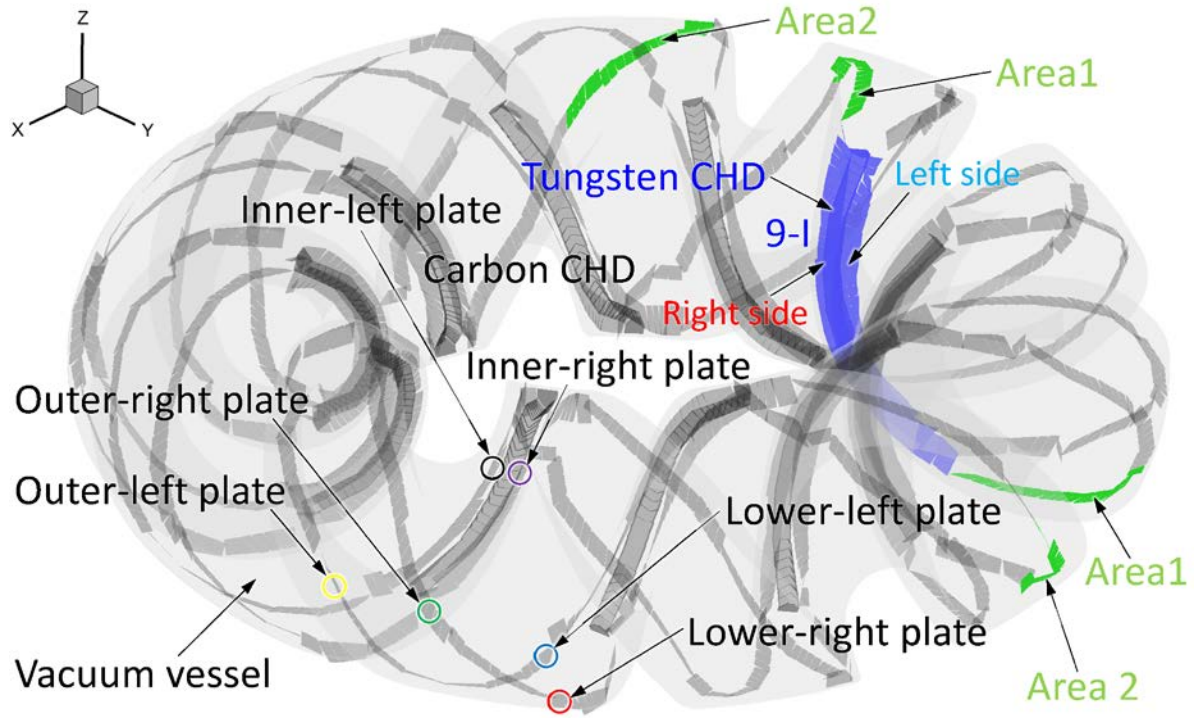

FIGURE 1 A three-dimensional full-tours model for the ERO2.0 simulation, which includes the closed helical divertor in the inboard side with the tungsten divertor plates in one helical section and the conventional carbon divertor plates in the other nine helical sections. Six representative divertor positions for carbon sources also are indicated as coloured circles.

ERO2.0 code. This code traces the trajectories of impurity atoms sputtered from the plasma facing components

and the trajectories of the impurity ions in the peripheral plasma using the ionization and recombination rates derived from the database on the Atomic Data and Analysis Structure (ADAS) [9]. The trajectories of impurity atoms and ions are followed with the full resolution of the gyro-motion with a perpendicular impurity ion diffusion coefficient of 1.0 m^2/s. It is assumed that the vacuum vessel is fully covered with carbon because it has been experimentally found that the surfaces around the divertor region are deposited by carbon dominant layers [10]. Tungsten erosion by background hydrogen and deuterium plasmas is found to be almost negligible because of the quite low sputtering yield at the typical incident energy of the background plasma (~100 eV) on the divertor plates in LHD [11, 12]. It is probable that the tungsten erosion is dominantly caused by the physical sputtering due to the intrinsic carbon ions in the peripheral plasma. The sputtering yield of tungsten by carbon ions is derived from the database calculated by a binary collision approximation code SDTrimSP [13] implemented in the ERO2.0 code. The fixed three-dimensional profile of background plasma parameters in the periphery (including the ergodic layer and divertor legs) is provided by a three-dimensional plasma edge simulation code (EMC3-EIRENE) [14, 15] in the typical magnetic axis configuration where the radial position of the magnetic axis R_{ax} is 3.60 m with the clockwise toroidal magnetic field direction. It has been found that the heat and particle fluxes in the CHD region in this magnetic configuration is much higher than those in the other divertor regions because the most of the magnetic field lines from the core plasma connect to the inboard side of the torus [16]. In this simulation, the plasma heating power P^{LCFS} and density at an inner plasma boundary at just inside of the Last Closed Flux Surface

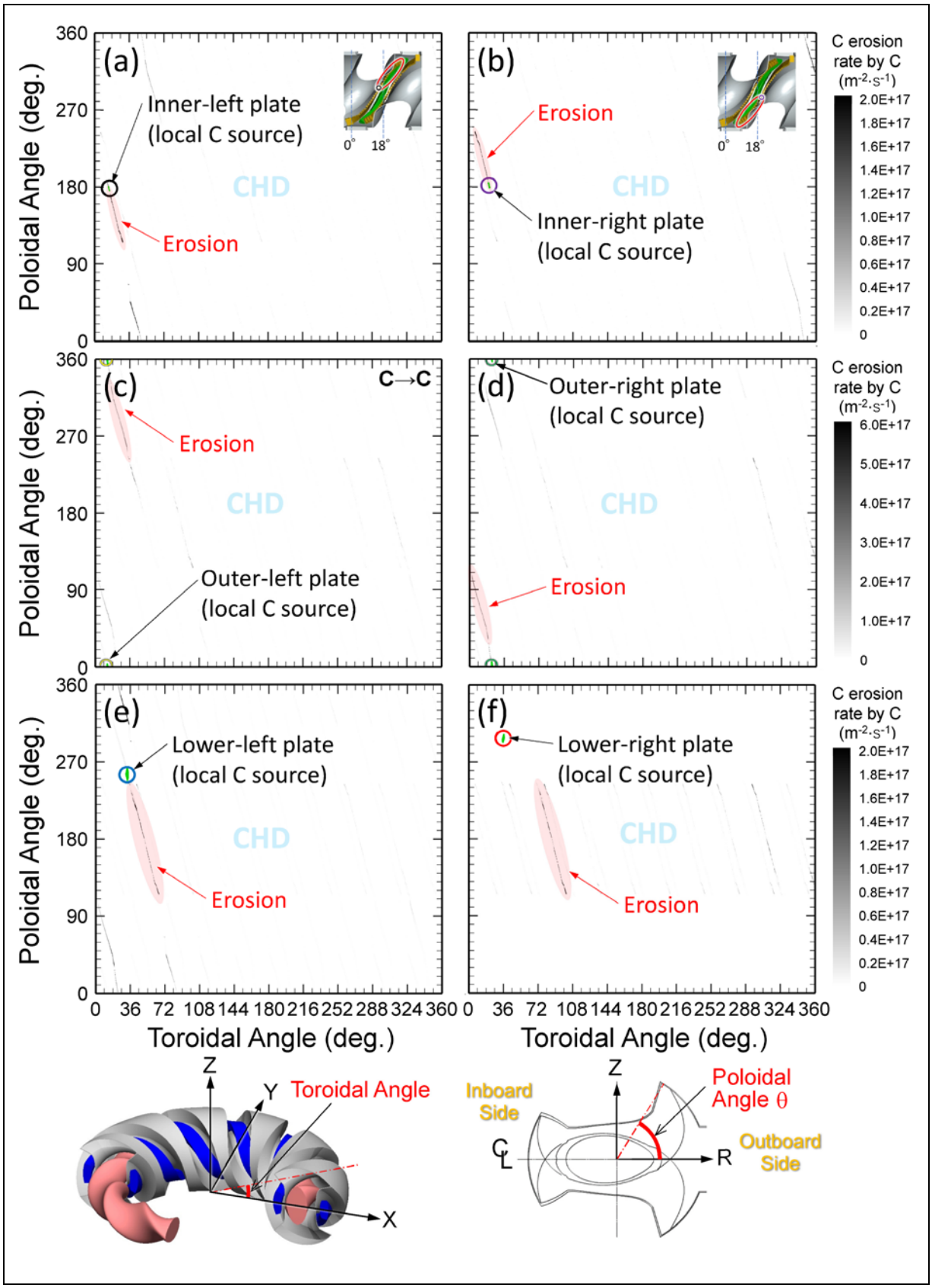
(a)
Inner-left plate
(local C source)
Erosion
CHD
(b)
Erosion
Inner-right plate
(local C source)
CHD
(c)
C→C
Erosion
Outer-left plate
(local C source)
CHD
(d)
Outer-right plate
(local C source)
Erosion
CHD
(e)
Lower-left plate
(local C source)
Erosion
CHD
(f)
Lower-right plate
(local C source)
Erosion
CHD
Poloidal Angle (deg.)
Toroidal Angle (deg.)
C erosion rate by C (m-2·s-1)
Z
Y
Toroidal Angle
X
Inboard Side
Poloidal Angle θ
Outboard Side
R

FIGURE 2 The ERO2.0 simulations of the toroidal and poloidal distribution of the carbon erosion rate due to the carbon ions produced by the physical and chemical sputtering at the position of the local carbon sources on divertor plates installed at the inner-left (a), inner-right (b), outer-left (c), outer-right (d), lower-left (e), and lower-right (f) side in the full carbon divertor configuration for R_{ax}=3.60m, P^{LCFS}=8 MW, and n_e^{LCFS}=4×10^{19} m^{-3}, respectively.

(LCFS) n_e^{LCFS} are set to be 8 MW and 4×10^{19} m^{-3}, respectively, which are typical values in standard plasma discharges in LHD. The profile of the plasma parameters (plasma density, ion and electron temperature, and the plasma flow velocity) are determined by fitting simulation results to measured electron density and temperature profiles in the peripheral plasma, in which the perpendicular particle and the thermal diffusion coefficients are assumed to be 0.5 and 1.0 m^2/s, respectively. When the impurity ions tracked in the ERO2.0 code reach the inner plasma boundary, new impurity ions are regenerated at random positions on the inner boundary, which is an adequate measure for the impurity transport in the core plasma because of the presence of nested magnetic flux surfaces in this area.

3 THE SIMULATION OF THE TOROIDAL AND POLOIDAL DISTRIBUTION OF THE EROSION ON THE DIVERTOR PLATES IN THE CASE OF LOCAL CARBON SOURCES

For finding an effective measure to suppress the tungsten erosion by incident carbon ions onto the tungsten coated divertor plates, the position of the carbon sources leading to the tungsten erosion has to be identified. Thus, in the ERO2.0 simulation, six local carbon sources are assumed for investigating the toroidal and poloidal distribution of the erosion on the divertor plates induced by the carbon ions which are produced by sputtering due to the background plasma at the carbon sources. The poloidal positions for the local carbon sources are set in three poloidal positions (inboard, lower, and outboard side of the torus). The two rows of the divertor plates are installed on the surface of the vacuum vessel along the two strike points between two helical coils. Therefore, two carbon sources (left and right) are additionally set on the divertor plates at the three poloidal positions as presented as coloured circles in Figure 1. In this simulation, a full carbon divertor configuration is assumed for the simple calculation, and carbons are produced by the physical and chemical sputtering due to the background deuterium plasma only at a divertor plate installed at the position of one of the local carbon sources.

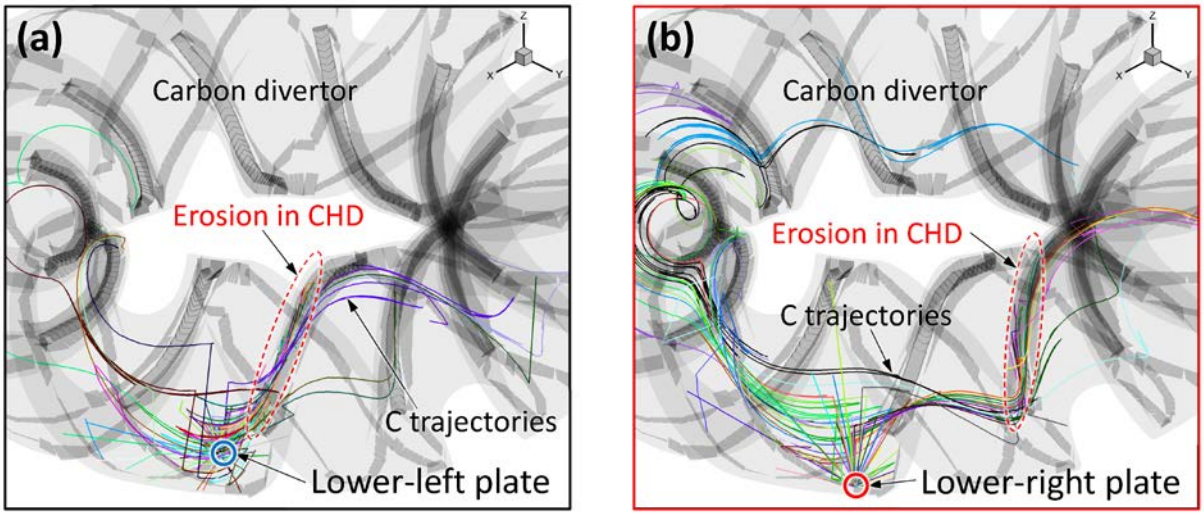

FIGURE 3 The ERO2.0 simulation results of typical trajectories of carbon atoms and ions produced by the physical and chemical sputtering by the background deuterium plasma for the local carbon source on a divertor plate in the lower-left (a) and lower-right side (b) for R_{ax}=3.60m, P^{LCFS}=8 MW, and n_e^{LCFS}=4×10^{19} m^{-3}, respectively.

Figure 2 summaries the toroidal and poloidal distribution of the carbon erosion rate on the divertor plates for each of the six local carbon sources, in which the simulations correspond to so-called “the first time step calculations” in ERO2.0. The erosion is induced by the carbon ions originated from the carbon atoms sputtered at the local carbon sources for the typical plasma discharge condition (R_{ax}=3.60 m, P^{LCFS}=8 MW, and n_e^{LCFS}=4×10^{19} m^{-3}). The simulations (shown in Figure 2 (a) and (b)) indicate that, for the local carbon sources in the inner-left and the inner-right side, the erosion is localized in the CHD region (120°<θ<240° where θ is a poloidal angle) at the helical section where the local carbon sources exist (shown as transparent red areas). These results elucidate that the carbons produced by the sputtering at the CHD region in a helical section do not give rise to the erosion in the other nine helical sections. Figure 2 (c) gives the erosion profile for the local carbon source at the outer-left side,

indicating the high erosion in the outer-lower side close to the carbon source. On the other hand, for the local carbon source at the outer-right side (illustrated in Figure 2 (d)), the simulation presents the erosion in the outer-upper side near the carbon source. These differences of the erosion profile are explained by the opposite plasma flow direction on the divertor legs close to the two carbon sources [17]. Figure 2 (e) shows the erosion profile for the local carbon source at the lower-left side, in which the erosion is high on the divertor plates along the left row in the CHD region near the carbon source. On the other hand, for the local carbon source in the lower-right side, the erosion is observable in the CHD region in the helical section far from the local carbon source by one helical section (36° in toroidal direction) as shown in figure 2 (f).

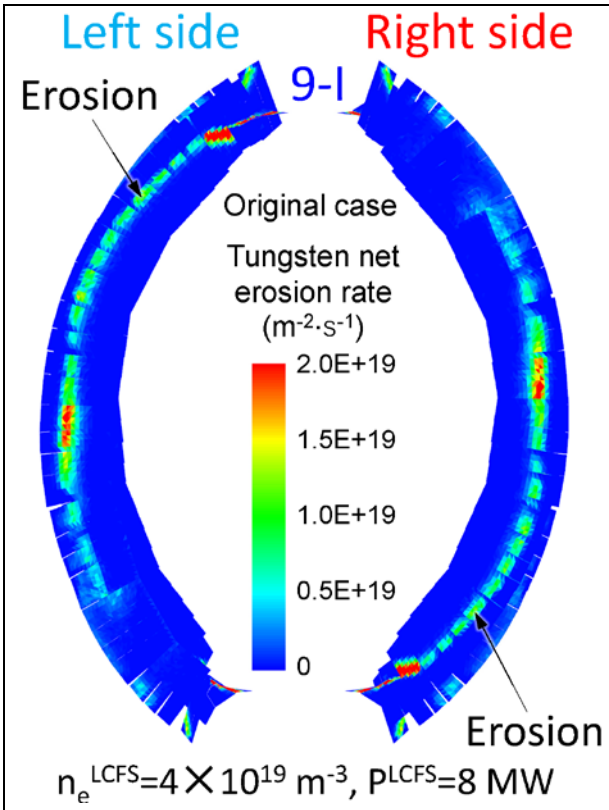

FIGURE 4 The simulation of the net tungsten erosion profile on the tungsten divertor plates in the left and right row in the CHD region calculated by the ERO2.0 code using the full-torus model for R_{ax}=3.60 m, P^{LCFS} =8 MW, and n_e^{LCFS}=4×10^{19} m^{-3}.

Figure 3 (a) and (b) illustrate the ERO2.0 simulation results of the typical trajectories of carbon atoms and ions produced by sputtering by the background plasma for the local carbon source at a divertor plate in the lower-left and lower-right sides, respectively. The simulations demonstrate that the carbon atoms produced by the sputtering at the local carbon sources reach the LHD peripheral plasma, and they are ionized in the plasma near the position of the local carbon sources. These carbon ions are transported to the CHD region along the magnetic field lines by the effect of the plasma flow in the peripheral plasma. For the local carbon source at the lower-left side, the carbon ions give rise to the erosion on the divertor plates in the CHD region in the adjacent helical section as shown in Figure 3 (a). On the other hand, for the local carbon source at the lower-right side (Figure 3 (b)), the carbon ions contribute to the erosion in the CHD region locating far from the carbon source by one helical section. This is because of the magnetic field line geometry in the LHD peripheral plasma between

the position of the carbon source and the CHD region. The ERO2.0 simulations demonstrate that the reduction of the sputtering on the divertor plates installed in the lower-left and lower-right sides, which are defined as ‘critical divertor areas’, is essential for suppressing the erosion on the divertor plates in the CHD region.

4 THE SIMULATION OF TUNGSTEN EROSION IN THE CLOSED HELICAL DIVETOR REGION

The simulation for calculating the tungsten erosion profile in the CHD region was performed using the full-torus model including the tungsten divertor plates in one helical section shown in Figure 1. Figure 4 gives the simulation result of the net tungsten erosion profile on the tungsten divertor plates in the left and right row for R_{ax}=3.60 m, P^{LCFS}=8 MW and $n_e^{LCFS}=4\times10^{19}$ m^{-3}. It indicates the erosion dominant areas along the strike points on the tungsten divertor plates in the upper-left and lower-right sides. The simulation result is consistent with the observed erosion profile of the tungsten layers coated on the divertor plates which was analysed using an imaging plate technique [18]. This technique revealed that about 50% of the surface on the tungsten coated divertor plates at the strike points was erosion dominant area [7]. This consistency suggests that the ERO2.0 code is applicable to the prediction of the tungsten erosion profile. As mentioned in the previous section, the carbons sputtered in the critical divertor areas has to be reduced for suppressing the tungsten erosion in the CHD region. Considering the up-down

symmetry of the divertor configuration, there are totally four critical divertor areas which additionally includes an upper-right divertor plate adjacent to the tungsten CHD region, and an upper-left divertor plate locating apart from the tungsten CHD region by one helical section. The lower-right and upper-left divertor areas adjacent to the tungsten divertor region are defined as ‘area 1’ in the simulation, and the lower-left and upper-right divertor areas locating apart from the tungsten CHD region by one helical section are names as ‘area 2’ as indicated as green divertor plates in Figure 1. In the ERO2.0 simulation, the carbon divertor plates in the area 1 and 2 are replaced to the tungsten ones for investigating the suppression of the tungsten erosion by reducing the carbon sputtering at the two critical divertor areas. Figure 5 gives the total tungsten net erosion rate in the tungsten CHD region in the following three cases. The first column (the left bar) represents the tungsten erosion rate in the original configuration in which the tungsten divertor plates are installed in the CHD region in one helical section. The second column (the middle bar) indicates the tungsten erosion rate in the case where the carbon divertor plates in the area 1 are replaced to the tungsten ones. The third column (the right bar) presents the tungsten erosion rate when the carbon divertor plates in area 1 and 2 are changed to the tungsten ones. Figure 5 proves that the replacement of the carbon divertor plates to the tungsten divertor ones in the two critical divertor areas is effective to suppress the tungsten erosion rate by about 30% in the CHD region.

5 SUMMARY

In LHD, the upgrade to the tungsten divertor configuration from the conventional carbon divertor ones has now progressed step by step. The exfoliation and erosion of the tungsten coated layers on the divertor plates in the CHD region in one helical section were found after the experimental campaign. For identifying the position of the carbon sources leading to the tungsten erosion, the toroidal and poloidal distribution of carbon erosion on the divertor plates induced by the carbons produced by sputtering due to the background plasma was investigated using the ERO2.0 code, in which the six local carbon sources are assumed in the full-torus carbon divertor configuration. The simulation reveals that the carbon divertor plates installed at the lower and upper side are the carbon sources giving rise to erosion in the CHD region. Tungsten erosion profile on the divertor plates in the CHD region was calculated by the ERO2.0 code using the full-torus model including the tungsten divertor plates installed in one helical section. The simulation of the tungsten erosion profile is consistent with the observation, which proves that the ERO2.0 code can be applied to the prediction of the tungsten erosion profile in the divertor region. The simulation demonstrates that the replacement of the carbon divertor plates installed in the two critical divertor areas to the tungsten ones is an effective measure to suppress the tungsten erosion in the CHD region.

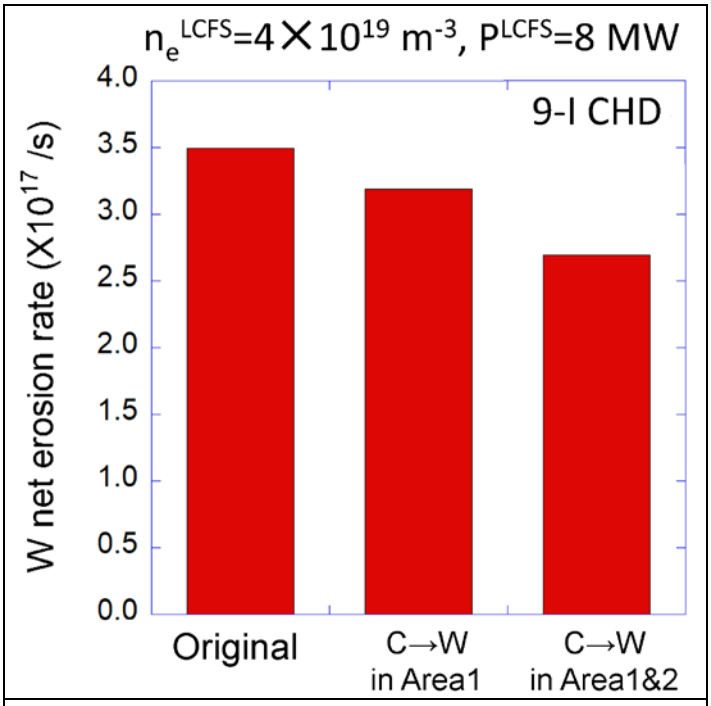

FIGURE 5 The total tungsten net erosion rate in the CHD region in the three different divertor configuration cases for R_{ax}=3.60m, P^{LCFS} =8 MW and $n_e^{LCFS}=4\times10^{19}$ m^{-3}.

ACKNOWLEDGEMENTS

This work is performed under the auspices of the NIFS Collaboration Research program (NIFS20KNSP007). One of the authors (M. S.) would like to thank Y. Feng for permission to use the EMC3-EIRENE. He is also grateful for the computational resources of the plasma simulator in NIFS. This work is also supported by JSPS KAKENHI Grant Numbers 18H01203.

REFERENCES

[1] G. De Temmerman, T. Hirai, R. A. Pitts, Plasma Phys. Control. Fusion **2018**, 60, 044018.

[2] R. A. Pitts, X. Bonnin, F. Escourbiac, H. Frerichs, J. P. Gunn, T. Hirai, A. S. Kukushkin, E. Kaveeva, M. A. Miller, D. Moulton, V. Rozhansky, I. Senichenkov, E. Sytova, O. Schmitz, P. C. Stangeby, G. De Temmerman, I. Veselova, S. Wiesenk, Nucl. Mater. Energy **2019**, 20, 100696.

[3] Y. Takeiri, T. Morisaki, M. Osakabe, M. Yokoyama, S. Sakakibara, H. Takahashi, Y. Nakamura, T. Oishi, G. Motojima, S. Murakami, K. Ito, A. Ejiri, S. Imagawa, S. Inagaki, M. Isobe, S. Kubo S. Masamune, T. Mito, I. Murakami, K. Nagaoka, K. Nagasaki, K. Nishimura, M. Sakamoto, R. Sakamoto, T. Shimozuma, K. Shinohara, H. Sugama, K. Y. Watanabe, J. W. Ahn, N. Akata, T. Akiyama, N. Ashikawa, J. Baldzuhn, T. Bando, E. Bernard, F. Castejón, H. Chikaraishi, M. Emoto, T. Evans, N. Ezumi, K. Fujii, H. Funaba, M. Goto, T. Goto, D. Gradic, Y. Gunsu, S. Hamaguchi, H. Hasegawa, Y. Hayashi, C. Hidalgo, T. Higashiguchi, Y. Hirooka, Y. Hishinuma, R. Horiuchi, K. Ichiguchi, K. Ida, T. Ido, H. Igami, K. Ikeda, S. Ishiguro, R. Ishizaki, A. Ishizawa, A. Ito, Y. Ito, A. Iwamoto, S. Kamio, K. Kamiya, O. Kaneko, R. Kanno, H. Kasahara, D. Kato, T. Kato, K. Kawahata, G. Kawamura, M. Kisaki, S. Kitajima, W.H. Ko, M. Kobayashi, S. Kobayashi, T. Kobayashi, K. Koga, A. Kohyama, R. Kumazawa, J.H. Lee, D. López-Bruna, R. Makino, S. Masuzaki, Y. Matsumoto, H. Matsuura, O. Mitarai, H. Miura, J. Miyazawa, N. Mizuguchi, C. Moon, S. Morita, T. Moritaka, K. Mukai, T. Muroga, S. Muto, T. Mutoh, T. Nagasaka, Y. Nagayama, N. Nakajima, Y. Nakamura, H. Nakanishi, H. Nakano, M. Nakata, Y. Narushima, D. Nishijima, A. Nishimura, S. Nishimura, T. Nishitani, M. Nishiura, Y. Nobuta, H. Noto, M. Nunami, T. Obana, K. Ogawa, S. Ohdachi, M. Ohno, N. Ohno, H. Ohtani, M. Okamoto, Y. Oya, T. Ozaki, B.J. Peterson, M. Preynas, S. Sagara, K. Saito, H. Sakaue, A. Sanpei, S. Satake, M. Sato, T. Saze, O. Schmitz, R. Seki, T. Seki, I. Sharov, A. Shimizu,

M. Shiratani, M. Shoji, C. Skinner, R. Soga, T. Stange, C. Suzuki, Y. Suzuki, S. Takada, K. Takahata, A. Takayama, S. Takayama, Y. Takemura, Y. Takeuchi, H. Tamura, N. Tamura, H. Tanaka, K. Tanaka, M. Tanaka, T. Tanaka, Y. Tanaka, S. Toda, Y. Todo, K. Toi, M. Toida, M. Tokitani, T. Tokuzawa, H. Tsuchiya, T. Tsujimura, K. Tsumori, S. Usami, J. L. Velasco, H. Wang, T. H. Watanabe, T. Watanabe, J. Yagi, M. Yajima, H. Yamada, I. Yamada, O. Yamagishi, N. Yamaguchi, Y. Yamamoto, N. Yanagi, R. Yasuhara, E. Yatsuka, N. Yoshida, M. Yoshinuma, S. Yoshimura, Y. Yoshimura, Nucl. Fusion **2017**, 57, 102023.

[4] M. Shoji, M. Kobayashi, S. Masuzaki, A. Iwamae, T Watanabe, H Yamada, A. Komori, Plasma and Fusion Res. **2008**, 3, S1038.

[5] M. Shoji, S. Masuzaki, M. Kobayashi, H. Funaba, T. Morisaki, H. Yamada, the LHD Experiment Group, J. Nucl. Mater. **2013**, 438, S559.

[6] M. Tokitani, S. Masuzaki, T. Murase, the LHD Experiment Group, Nucl. Mater. Energy **2019**, 18, 23.

[7] G. Motojima, S. Masuzaki, M. Kobayashi, T. Oishi, G. Kawamura, M. Shoji, Y. Hamaji, M. Kobayashi, M. Tokitani, T. Morisaki, Y. Takeiri, the LHD Experiment Group, presented at 28th IAEA Fusion Energy Conference 2020, EX/P6-22, Effects of partially installed tungsten coated divertor tiles on the LHD plasma and plasma-wall interactions, Virtual Event, (May, 2021).

[8] J. Romazanov, S. Brezinsek, D. Borodin, M. Groth, S. Wiesen, A. Kirschner, A. Huber, A. Widdowson, M. Airila, A. Eksaeva, I. Borodkina, Ch. Linsmeier, JET Contributors, Nucl. Mater. Energy **2019**, 18, 331.

[9] The ADAS Project, ADAS Manual 2.6, https://www.adas.ac.uk/manual.php, August, 2021.

[10] G. Motojima, N. Yoshida, S. Masuzaki, R. Sakamoto, M. Tokitani, H. Tanaka, T. Murase, D. Nagata, K. Matsumoto, M. Miyamoto, M. Yajima, M. Sakamoto, H. Yamada, T. Morisaki, the LHD Experiment Group, Nucl. Mater. Energy **2017**, 12, 1219.

[11] J. Roth, E. Tsitrone, T. Loarer, V. Philipps, S. Brezinsek, A. Loarte, G. F. Counsell, R. P. Doerner, K. Schmid, O. V. Ogorodnikova1, R. A. Causey, Plasma Phys. Control. Fusion **2008**, 50, 103001.

[12] S. Masuzaki, T. Morisaki, N. Ohyabu, A. Komori, H. Suzuki, N. Noda, Y. Kubota, R. Sakamoto, K. Narihara, K. Kawahata, K. Tanaka, T. Tokuzawa, S. Morita, M. Goto, M. Osakabe, T. Watanabe, Y. Matsumoto, O. Motojima, the LHD Experimental group, Nucl. Fusion **2002**, 42 750.

[13] W. Möller, W. Eckstein, J. P. Biersack, Comput. Phys. Commun. **1988**, 51, 355.

[14] Y. Feng, F. Sardei, P. Grigull, K. McCormick, J. Kisslinger, D. Reiter, Y. Igitkhanov, Plasma Phys. Control. Fusion **2002**, 44, 611.

[15] G. Kawamura, Y. Feng, M. Kobayashi, M. Shoji, T. Morisaki, S. Masuzaki, Y. Tomita, Contrib. Plasma Phys. **2014**, 54, 437.

[16] M. Shoji, M. Kobayashi, S. Masuzaki, T. Watanabe, H. Yamada, A. Komori, LHD experimental groups, J. Nucl. Mater. **2009**, 390-391, 490.

[17] M. Shoji, S. Masuzaki, T. Morisaki, M. Tokitani, R. Sakamoto, H. Yamada, the LHD Experiment Group, J. Nucl. Mater. **2011**, 415, S557.

[18] S. Masuzaki, M. Yajima, K. Ogawa, G. Motojima, M. Tanaka, M. Tokitani, M. Isobe, T. Otsuka, the LHD Experiment Group, Nucl. Mater. Energy 26, 100884 (2021).